Superluminal sheath-field expansion and fast-electron-beam divergence measurements in laser-solid interactions

C. P. Ridgers,[1] M. Sherlock,[1] R. G. Evans,[1] A. P. L. Robinson,[2] and R. J. Kingham[1]
[1]*Blackett Laboratory, Imperial College of Science Technology and Medicine, London, SW7 2AZ, United Kingdom*
[2]*Central Laser Facility, STFC Rutherford-Appleton Laboratory, Chilton, Didcot, Oxfordshire, OX11 0QX, United Kingdom*
(Received 6 June 2010; revised manuscript received 23 December 2010; published 8 March 2011)

We show that including a sufficient description of the target's rear surface significantly affects the interpretation of a wide range of laser-solid experiments. A simple Debye sheath model will be shown to be adequate. From this the sheath field responsible for ion acceleration has been shown to expand at superluminal speeds, leading to very large ion-emission regions on the target's rear surface; a new explanation for the dynamics of the ion-accelerating sheath field accounts for this observation and demonstrates the inaccuracy of measuring the angular divergence of the injected electron beam, crucial to fast ignition, from the lateral extent of the ion emission. However, it is shown that on careful probing the sheath field can provide unique insight into details of the fast electron's distribution function. The relative merits of probing other physical quantities has been examined. The width of the background temperature spot overestimates the divergence by a factor of 2 unless electron recirculation is prevented.

DOI: 10.1103/PhysRevE.83.036404 PACS number(s): 52.57.−z, 41.75.Ak, 52.50.Jm, 52.65.Ff

I. INTRODUCTION

The interaction between high-intensity lasers and solid targets is of primary importance in current laser-plasma research. A full understanding of such interactions is crucial to fast-ignition inertial confinement fusion, which offers the promise of thermonuclear ignition with less driver laser energy than standard central hot-spot ignition [1], and in the acceleration of ion beams from solid targets [2]. In particular, the beam of relativistic fast electrons generated when the high-intensity laser strikes the solid must be characterized. Characterizing the angular divergence of the fast-electron beam is of particular importance in determining the viability of the cone-guided fast-ignition scheme where fast electrons emitted from the tip of a gold cone heat and ignite a precompressed pellet of deuterium-tritium fuel. The angular divergence of the electron beam is critical in determining the flux of fast electrons reaching the core, and hence if ignition is possible [3]. Experimental studies to this aim frequently rely on rear-surface probing of densities, temperatures, or electric fields [4–7]. However, numerical simulations relevant to these experiments have rarely treated the rear surface sufficiently in two dimensions (2D); the effect of including the rear surface on the interpretation of experimental measurements has yet to be elucidated.

It will be shown that measurements of the half-angle based on the temperature can be in significant error unless care is taken. This error is a direct result of processes occurring at the rear of the target, namely, the generation of a sheath electric field when fast electrons leave the target and enter the vacuum region behind it. In order to prevent the target charging up by fast electrons escaping it, the field quickly becomes strong enough to reflect almost all of the incoming fast-electron beam. Therefore fast electrons recirculate through the target many times. This will be shown to lead to a broad temperature profile along the rear surface that, when assuming the electrons are moving ballistically, gives an apparent half-angle of divergence of 70°, compared to the value of 28° injected in the simulations [6]. Such a discrepancy could make the difference to the perceived viability of cone-guided fast ignition. Furthermore, it will be shown that the lateral extent of the sheath is dramatically different to that of the fast electrons on the rear surface; thus a naive interpretation of measurements of the size of the sheath or ion-emission region (ions are accelerated by the sheath) will yield a very poor measurement of the angular divergence.

However, some degree of characterization of the beam is possible by probing the sheath. This will be explained by the development of a simple 2D Debye-sheath model, with which we will show that the sheath field is sensitive to a wide dynamic range in the fast-electron number density—in particular, those injected with large divergence angles. From direct probing of the sheath, in combination with measuring temperature (where care has been taken to suppress volumetric heating of the target by recirculating electron currents) and density (inferred from transition radiation or K_α from tracer layers [4–6,8]), we may infer not only the average angular divergence of the beam, but go some way to constraining its angular distribution function. Furthermore, the sheath potential will be shown to depend only on the fast electron's average energy and so can be used to measure the average energy of the fast electrons and its dependence on the injection angle.

In target-normal sheath ion acceleration (TNSA), ions are accelerated by a sheath electric field at the rear surface of the target. This field has been observed in experiments to spread very rapidly along the target's rear surface, giving an ion-emitting region larger than is consistent with other measures of electron-beam divergence [9–12]. The cause of this spreading is an open question; an appropriate description of the rear surface must be included in the numerical modeling to understand TNSA. The 2D ion-static sheath field (i.e., that generated when the ions are immobile) model discussed in the context of characterizing the fast-electron beam will be useful to this end; this is, after all, the field that initiates TNSA. The sheath will be shown to expand along the target's surface superluminally, leading to the large ion-emitting region observed experimentally. Indeed, the observation of such superluminal expansion would provide an excellent

confirmation of the validity of the model. The sheath model derived here has the potential to explain other curious observations relating to TNSA, such as the insensitivity of ion-spot size to target thickness.

In this paper solid density plasmas were simulated with the Vlasov code FIDO [13]. This code has been recently developed to simulate realistic target edges in order to study TNSA and rear-surface effects. In principle, particle-based codes can simulate such edges, however, in 2D they lack the number of particles to have a dynamic range large enough to capture the generation of a Debye sheath by the few electrons far from the laser spot [14]; this will be shown to be crucial for modeling the Debye sheath in 2D. FIDO uses the hybrid approximation [3,15], solving the Vlasov equation for the fast electrons generated by the high-intensity laser and using a fluid treatment for the cold electrons that make up the target.

The outline of the rest of the paper is as follows. In Sec. II the simulation code FIDO will be described and details of the simulation parameters given. It will next be necessary to derive the sheath model; this is done in Sec. III using an electrostatic model. When discussing the sheath model particular attention will be paid to deriving scaling laws relating the peak electric field, scale length and the resulting potential to the number density of fast electrons in the incoming beam and their energy, and the speed at which the sheath spreads transversely along the target's rear surface. In deriving the sheath model, sheath magnetic fields are neglected; this will be justified in Sec. IV. A unique model for the spreading of the sheath will be derived and will be shown to be more important than the previous explanations reliant on recirculation or B fields.

Once the sheath model is established, its effect on the interpretation of rear-surface measurements will be discussed in Sec. V. We will see in Sec. V A that the rapid (superluminal,- as seen in Sec. III C) spreading of the sheath field along the target means that the vast majority of fast electrons striking the rear surface are reflected; i.e., there are strong recirculating currents throughout the target. It will be shown that the resultant broadening of the temperature profile on the rear can be removed by suppressing recirculation, giving a good measure of the angular divergence. In order to constrain the angular distribution of the fast electrons further, it will be shown that direct probing of the sheath field is useful—this will be demonstrated in Sec. V B. Using the scaling laws derived using the sheath model in Sec. III, it will be shown that measuring the sheath's maximum value and scale length provides sufficient information to reconstruct the number of electrons injected with a given angle. In Sec. VI B the consequences of the sheath model for TNSA ion acceleration will be discussed, with particular reference to the rapid spreading of the sheath predicted by the model.

II. NUMERICAL SIMULATIONS

A. Numerical model

The fast electrons were modeled by solving the Vlasov equation,

$$\frac{\partial f}{\partial t} + \mathbf{v}\cdot\frac{\partial f}{\partial \mathbf{r}} + \mathbf{F}\cdot\frac{\partial f}{\partial \mathbf{p}} = \frac{\delta f_{\mathrm{inj}}}{\delta t}. \quad (1)$$

f is the distribution function of the fast electrons in position $\mathbf{r}$ and momentum $\mathbf{p}$ space. $\mathbf{F}$ is the Lorentz force, i.e., $\mathbf{F} = -e(\mathbf{E} + \mathbf{v}\times\mathbf{B})$. The distribution function f is 6D, making any numerical solution to Eq. (1) prohibitively computationally costly. This is usually overcome by expanding f in basis functions in a solid angle in momentum space (for example, the spherical harmonics [16] or the Cartesian tensors [17]). This reduces the dimensionality of the problem to 3, but results in complicated, nonstandard equations. This is not done in the model used by FIDO. In the kinds of interactions discussed here the field configuration can be reduced to $\mathbf{E} = E_x\hat{\mathbf{e}}_x + E_y\hat{\mathbf{e}}_y$, $\mathbf{B} = B_z\hat{\mathbf{e}}_z$. In this case momentum space can be considered in cylindrical polar coordinates, with z as an ignorable coordinate, reducing the dimensionality to 4 and rendering numerical solution feasible (if costly). Further, because Eq. (1) is solved directly as a standard conservative advection equation, standard techniques may be employed, namely, the piecewise-parabolic method [18]. This method can handle very steep density gradients and enabled the solution of target edges. In addition, as f is a 4D phase fluid, we were able to resolve the effect of very low relative particle densities on the generation of the sheath field; this would be difficult to achieve with a particle-based code.

The fast population was injected using the function

$$f_{\mathrm{inj}}(p,\theta) \propto \exp\left[-\left(\frac{E-E_0}{2E_0}\right)^2\right]\exp\left[-\left(\frac{\theta}{\theta_{1/2}}\right)^2\right]. \quad (2)$$

This was derived by Sherlock [13]. Here $E_0 = 1$ MeV and $\theta_{1/2} = 28^\circ$ was used to parametrize the angle of injection. Note that Sherlock described 1D absorption and found a super-Gaussian distribution in θ; in hybrid Particle-in-Cell simulations it is more usual to use a Gaussian dependence [19], the difference being owing to 2D effects or numerical heating. The more standard Gaussian dependence is used here. Collisions were neglected for the fast electrons as their scattering time from the ions was 1.6 ps, which was longer than the simulation time. The bulk (cold) target electrons affected the fast electrons indirectly by providing a return current $\mathbf{j}_R = \sigma\mathbf{E}$, where σ is the Spitzer electrical conductivity [20]. Note that this conductivity is only strictly valid at background temperatures over 100 eV. Using the Milchberg resistivity [21] increased the collimating B field inside the target, but as the beam was already collimated this made no significant difference to its propagation and interaction with the rear surface. Ionization dynamics was not included and could act as an energy sink, changing the temperature, resistivity and degree of collimation inside the target; this will not dramatically affect the physics discussed here, which is concerned with the generation of the sheath outside the target.

B. Simulation parameters

The target was fully ionized ($Z = 13$) solid aluminum (density 2.7 g cm^{-3}) and its thickness was 10 μm. The laser intensity I_0 was 2.0×10^{19} W cm^{-2}, giving an average injected energy of 1 MeV, and the absorption fraction was set to 0.3. The laser spot was Gaussian with width $\lambda_L = 3.6$ μm, i.e., $I = I_0 e^{-(x/\lambda_L)^2}$. The electron beam was injected moving in the $+y$ direction over a thin 0.5-μm layer in y. The spatial

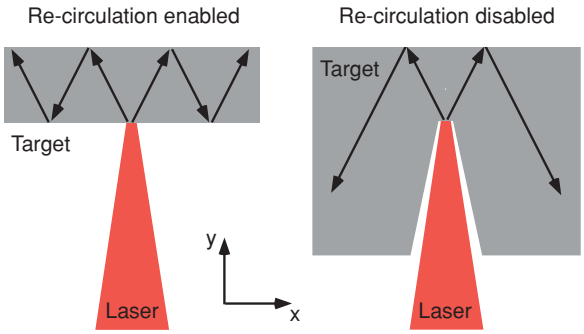

FIG. 1. (Color online) The two types of targets considered in this paper.

domain was resolved with cells 0.5 μm $\times$ 0.5 μm inside the target (-120 μm $\leqslant x \leqslant$ 120 μm, $0 \leqslant y \leqslant$ 10 μm). Outside the target the cell size for adequate resolution of the sheath was small (20 cells per fast-electron Debye length, 0.2 μm) so that 2D simulations including the sheath were limited to 100 fs—small compared to typical experiments but sufficient to measure the field's expansion speed. To overcome this, 1D simulations were performed in order to derive scaling laws for the peak sheath field and its potential with the fast-electron current $j_y = -en_f c$; these were then used in conjunction with 2D simulations where the rear surface was not directly modeled (but treated as a reflecting boundary) to reconstruct the expected sheath fields after longer times.

In order to determine if an improved correspondence between the temperature and density measurements made on the rear surface and the actual size of the beam inside the target could be achieved (and so the accuracy of estimates of its initial angular divergence improved), 2D simulations were performed with refluxing suppressed; recirculation was found to be crucial in determining the width of profiles on the rear. This was done by stretching the numerical grid in the $-y$ direction, allowing the fast electrons to escape to $y \to -\infty$, as was achieved in the experimental arrangement of Lancaster *et al.* [6]; the targets used in the experiment are illustrated in Fig. 1, where that on the left-hand side is the standard target and that on the right-hand side is shaped to suppress recirculation. This provides a numerical test of the conclusion of Lancaster *et al.* that suppressing refluxing by using targets shaped as the left-hand one in Fig. 1 allows for an accurate measurement of the beam's injection angle.

III. SHEATH-FIELD FORMATION AND EXPANSION

Inside the target the current from the fast-electron beam was canceled out by a return current drawn from the cold background electrons (in order to maintain quasineutrality). When the density of the background plasma dropped below the density of the beam, i.e., below the critical density, this cancellation was no longer possible. In this case the Ampere-Maxwell law, $\partial E_y/\partial t = -j_y/\epsilon_0$ (where we have ignored $\nabla \times \mathbf{B}$; see Sec. IV), predicts the rapid growth of a large electric field—the sheath field. Thus when the fast electrons reached the rear surface of the target and entered the vacuum, they generated a sheath electric field in the y direction. Experimentally, such sheath fields are seen to move very rapidly along the target surface [10,22], so therefore there must be a j_y sufficient to generate such fields over a large area on the rear surface. This has so far been explained by recirculating currents leading to electrons present far from the injection region or by large magnetic fields on the rear surface causing an "$\mathbf{E} \times \mathbf{B}$" drift along this surface [23]. We will show that a unique mechanism dominates that is reliant on electrons on their first pass through the target. The weak dependence of the sheath field on the incoming j_y meant that the few electrons that were injected with large angles could generate large sheath fields.

First, the formation of the sheath field will be discussed in 1D. This will then be used to derive a scaling law for the maximum value of the electric field (and the resulting potential) in its formation and saturated phases along with the formation time (i.e., the time to transition between these phases). These scalings will be tested in 2D over 100 fs and used to estimate the sheath field and potential after 1 ps.

A. 1D simulations

The dependence of the peak sheath field E_y^{peak} and the potential Φ on the incoming fast-electron number density was investigated in 1D owing to strong resolution constraints. The number density of injected fast electrons was set to different fractions n_f/n_{0f} of that calculated by the injection function n_{0f}. Two distinct regimes were observed. Initially, the field was not strong enough to reflect fast electrons—this is the *setup phase*. After a time scale of ω_{pf}^{-1} (ω_{pf} is the relativistic plasma frequency for the fast electrons) the field was sufficiently strong to reflect most of the electrons and a Debye sheath was set up—the *saturation phase*.

In the setup phase Ampere-Maxwell's equation can be integrated straightforwardly as j_y may be assumed constant:

$$\frac{\partial E_y}{\partial t} = -\frac{j_y}{\epsilon_0} = \frac{n_f e c}{\epsilon_0} \tag{3}$$

$$\Rightarrow E_y = \frac{n_f e c}{\epsilon_0} t. \tag{4}$$

The sheath potential Φ can be calculated by assuming that the electric field grows uniformly in the region over which the fast-electron beam has penetrated into the vacuum. Thus the scale length of the field is $L_E = ct$ and so

$$\Phi = -\int_0^{ct} dy'\, E_y^{\text{peak}} = -E_y^{\text{peak}} \int_0^{ct} dy' = -\frac{n_f e}{\epsilon_0}(ct)^2. \tag{5}$$

Therefore, in the setup phase,

$$E_y^{\text{peak}} \propto \frac{n_f}{n_{f0}}, \quad \Phi \propto \frac{n_f}{n_{f0}}. \tag{6}$$

These relations hold until the field becomes large enough to reflect a significant number of fast electrons; j_y can then not be assumed to be constant and the saturation phase is reached. In this phase the sheath field was found to fall off exponentially over the fast-electron Debye length—a Debye sheath was formed [24]:

$$E_y = E_y^{\text{peak}} \exp\left(-\frac{y'}{\lambda_{Df}}\right), \quad \lambda_{Df} = \left(\frac{\epsilon_0 T_f}{n_e e^2}\right)^{1/2}, \tag{7}$$

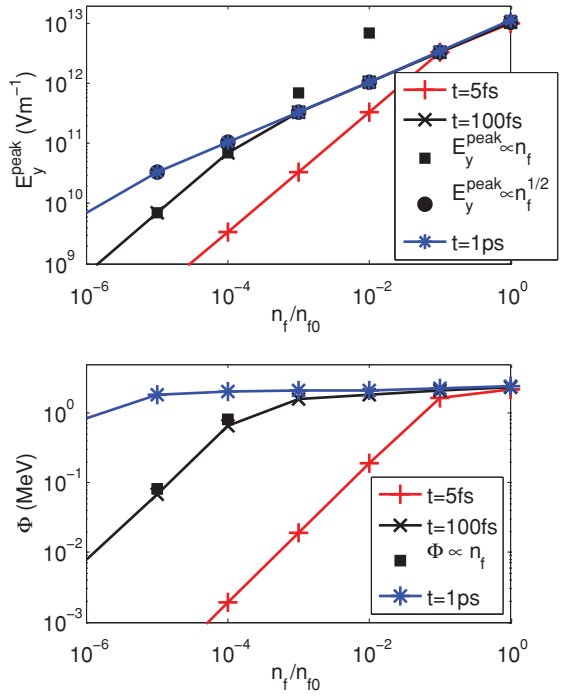

FIG. 2. (Color online) The peak sheath field (top) and potential (bottom) against the fractional number density of fast electrons injected in 1D simulations (n_f/n_{0f}) various times into the simulation.

where y' is the distance from the target edge. This sheath does an amount of work equal to the average energy of the injected beam T_f, i.e.,

$$\Phi = T_f = -\int_0^\infty E_y\, dy' \Rightarrow E_y^{\text{peak}} = \frac{T_f}{\lambda_{Df}} \propto \left(\frac{n_f}{n_{f0}}\right)^{1/2}. \quad (8)$$

Note that in the saturated phase Φ is independent of n_f and only depends on the energy of the fast electrons.

Validation of these analytical results was done with 1D FIDO simulations. Figure 2 shows the peak sheath field E_y^{peak} and the potential Φ against n_f/n_{0f} various times into the simulation; E_y^{peak} and Φ each display two distinct scalings with n_f/n_{f0}. As expected from the arguments given above, both E_y^{peak} and Φ scale linearly with n_f in the setup phase. In the saturation phase (reached after 1 ps for all n_f/n_{0f}) the potential was approximately constant falling from 2.4 to 1.8 MeV as the injected density dropped by five orders of magnitude and E_y^{peak} displayed the expected $n_f^{1/2}$ scaling.

The difference between the scalings at various times shown in Fig. 2 is that, for earlier times, the sheath is saturated only at large injected number density; the shift between setup and saturation phases occurs further to the right. At later times the sheath has entered the saturation phase at lower injected densities; the point delineating the two phases in Fig. 2 moves to the left. This can be understood by noting that if fewer electrons are injected the sheath's growth time will be longer (from the Ampere-Maxwell law the growth rate is proportional to the fast-electron current $\partial E_y/\partial t = -j_y/\epsilon_0$), the sheath will take longer to saturate and so will remain in the linear phase for longer.

We can quantify this by deriving an expression for sheath's saturation time τ_s. τ_s can be estimated by approximating the Ampere-Maxwell law to

$$\frac{E_y^{\text{peak}}}{\tau_s} = \frac{ecn_f}{\epsilon_0} \quad \Rightarrow \quad \tau_s = \frac{1}{\omega_{\text{pf}}}, \quad (9)$$

where ω_{pf} is the relativistic plasma frequency of the fast electrons. In Fig. 2 we see that after 5 fs all injected currents below 10^{-1} of the maximum were in the linear growth phase (i.e., $E_y, \Phi \propto n_f$); by 100 fs only fractional currents less than 10^{-4} were still in the linear phase. This behavior is well predicted by the saturation time in Eq. (9).

The fact that the potential of the sheath in the saturated phase was not equal to T_f but to some multiple of it can be explained by examining the structure of the sheath in the y direction. A plot of this profile is shown in Fig. 3. In the top plot we see that the sheath naturally separated into two regions: the *Debye sheath* where the field fell exponentially over a small spatial region ($\lambda_{Df} = 0.2\ \mu$m); and the *plateau*, where the field fell slowly for a large distance before rapidly falling to zero. The plateau was caused by electrons escaping the target before the sheath was set up. The sheath potential up to y', i.e., $-\int_0^{y'} E_y\, dy'$ is shown in the bottom plot. Here we see that the Debye part of the sheath had potential $\Phi \approx T_f$ (the Debye sheath ended at $y' \approx 0.2\ \mu$m). Therefore, the plateau was responsible for the excess potential. We will discuss the plateau further in a followup paper, where we will be interested in the energy of the escaping electrons. In this paper we will be interested in the Debye sheath, so $\Phi \approx T_f$ is valid.

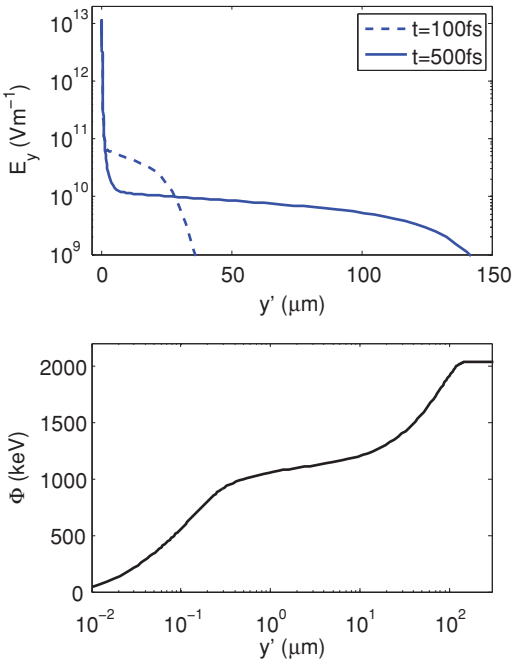

FIG. 3. (Color online) The sheath field 100 and 500 fs after the beam enters the vacuum (top). The potential of the sheath after 500 fs (bottom).

B. 2D simulations

The need to resolve the fast electron's Debye length limited 2D simulations of the sheath-field evolution to durations of 100 fs. These short-time-scale situations were sufficient to measure the expansion speed of the sheath. In addition, the scaling laws for the sheath field and potential developed in 1D in the last section can be extended to 2D. The 2D scaling laws allow predictions about the sheath field to be made based on the number density of fast electrons reaching the rear surface. After validating the 2D scaling laws using the short-time-scale 2D simulations, they can be used to predict the fields over longer time scales based on simulations of the interior of the target only (which do not suffer stringent resolution constraints).

First, we extend the scaling laws to 2D. The scaling laws in the setup phase can be derived using the Ampere-Maxwell law, noting that the current perpendicular to the surface is $j_y = |\mathbf{j}| \cos\theta$:

$$\frac{\partial E_y}{\partial t} = \frac{n_f e c}{\epsilon_0} \cos\theta \tag{10}$$

$$\Rightarrow E_y^{\text{peak}} \propto n_f t \cos\theta, \quad \Phi \propto n_f t^2 \cos\theta. \tag{11}$$

To derive the scaling law for the saturation phase in 2D it is necessary to account for the fact that the electrons have less momentum perpendicular to the surface as the angle of injection increases, and thus the sheath needs to do less work to reflect them. In the saturation phase we have

$$\Phi = T_{f\perp} = \gamma_\perp m_e c^2 \propto \cos\theta \tag{12}$$

$$\begin{aligned} E_y^{\text{peak}} \lambda_{Df} &= T_{f\perp}, \quad \lambda_{Df} \propto T_{f\perp}^{1/2} \propto (\cos\theta)^{1/2} \\ &\Rightarrow E_y^{\text{peak}} \propto T_{f\perp}^{1/2} \propto n_f^{1/2} (\cos\theta)^{1/2}, \end{aligned} \tag{13}$$

where we have assumed that the electrons are ultrarelativistic so their gamma factor resulting from momentum perpendicular to the surface $\gamma_\perp \approx (p_\perp / m_e c) \propto \cos\theta$.

These scaling laws have been used to calculate sheath field and potential profiles, labeled "theory" in the top plot in Fig. 4, which were compared to those from the 2D FIDO simulations, labeled "code" in the figure. The agreement was reasonable. Later evolution of the sheath can be estimated by constructing E_y and Φ from simulations with a reflective boundary at the target rear surface, using the scaling laws, as is shown in Fig. 4 (bottom). It can be seen that the lateral extent of the sheath would be very large (120 μm) compared to the beam width (20 μm) after only 285 fs. A large (80 μm) sheath potential would be seen even if recirculation was suppressed.

Using the short-time-scale 2D simulations the speed of the expansion was found to be superluminal initially, with the field expanding at a speed of $1.6c$, 10 μm along the rear surface, and to asymptotically approach c further along the rear surface; recirculating currents or B fields cannot cause the field to spread this rapidly, indirectly suggesting that they are not responsible for the spreading. The lower plot in Fig. 4 directly shows that disabling recirculation had little effect on the lateral-expansion speed of the front of the sheath, although recirculation did increase the magnitude of E_y and Φ behind the expanding front. Refluxing is not essential for large lateral expansion of the sheath.

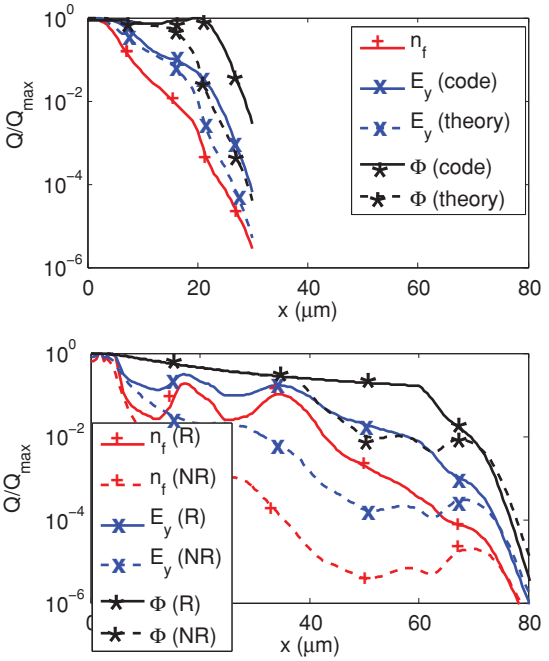

FIG. 4. (Color online) Fast-electron number density just inside and sheath field and potential just outside the target after 100 fs (top). Profiles outside the target constructed from current inside after 285 fs with (R) and without (NR) refluxing (bottom). The peak values are as follows: $n_f^{\text{peak}} = 2.0 \times 10^{27}$ m^{-3}, $E_y^{\text{peak}} = 8.1 \times 10^{12}$ V m^{-1}, and $\Phi^{\text{peak}} = 3.8$ MeV (top); $n_f^{\text{peak}} = 4.6 \times 10^{27}$ m^{-3} with refluxing and $n_f^{\text{peak}} = 2.4 \times 10^{27}$ m^{-3} without refluxing (bottom). $Q/Q_{\max}$ represents the normalized value of a general physical quantity.

C. Sheath expansion model

The 1D and 2D sheath-field simulation results may be brought together to propose a unique mechanism that supposes that electrons generate the field on their first pass through the target. The injected fast electron distribution goes as $\exp -(\theta/\theta_{1/2})^2$, so although the average is $\theta_{1/2} = 28^\circ$, the very weak dependence of Φ on n_f means that the few electrons injected with much larger angles can generate a large sheath field, causing it to spread far along the rear surface. This is illustrated in Fig. 5, the sheath field spreads up the target as

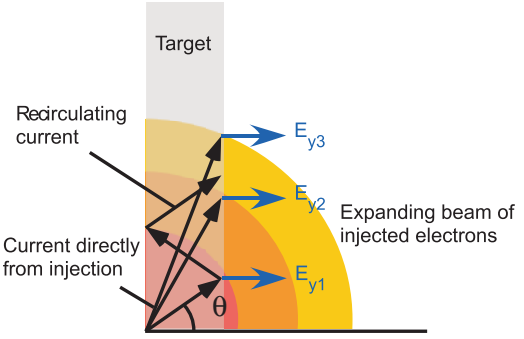

FIG. 5. (Color online) An illustration of the mechanism responsible for the lateral spreading of the sheath electric field responsible for TNSA. The sheath field spreads up the target with the increasing intersection of the expanding cloud of fast electrons and the plane of the rear.

fast electrons arrive from larger and larger injection angles, striking the rear surface and generating field $\mathbf{E}_{y1}$ followed by $\mathbf{E}_{y2}$ and finally $\mathbf{E}_{y3}$; recirculating currents enhance the sheath field behind the expanding front. The speed of expansion v_E is calculated as follows: The electrons injected into the target at a given time propagate through it along a half-cylindrical front of expanding radius; although the number density of fast electrons falls off rapidly as $\theta > \theta_0$, we have shown that the magnitude of the sheath field and its potential are insensitive to this—therefore the sheath field is generated as this cylinder intersects the rear of the target. v_E is given by determining the rate of change of the chord length formed by the intersection of the cylinder and the rear surface:

$$v_E = \frac{c}{\sin\theta} > c, \tag{14}$$

which is superluminal and consistent with the 2D simulation data, predicting a speed of $1.4c$, 10 μm along the rear surface. It should be noted that once the current of first-pass fast electrons drops below the level required to form the sheath in a reasonable time, refluxing electrons dominate the propagation of the sheath and the speed slows to $<c$.

IV. REAR-SURFACE MAGNETIC FIELD

An alternative explanation for the lateral expansion of the sheath field, $\partial E_y/\partial t = -j_y/\epsilon_0$, is that $\mathbf{E} \times \mathbf{B}$ drifts enhance the spreading of the electrons along the rear surface [23]. However, the rear-surface B field can be shown to be of marginal significance despite the fact that large magnetic fields (2000 T) were generated in the 2D simulations. First, we can give a simple order of magnitude explanation for this B field.

Assuming that the magnetic field is generated from $\nabla \times \mathbf{E}$ as the sheath field front moves by at speed $\approx c$, then if the front has a scale length L, the B field is generated over time $\tau = L/c$, therefore,

$$\frac{\partial \mathbf{B}}{\partial t} = -\nabla \times \mathbf{E}, \quad \frac{B}{\tau} \approx \frac{E}{L} \Rightarrow B \approx \frac{E}{c}, \tag{15}$$

$B = |\mathbf{B}|$, and $E = |\mathbf{E}|$. Figure 4 shows that the maximum value of the sheath E field was of the order of 10^{12} V m^{-1} over a wide region on the rear of the target. From this the above scaling predicts $B \approx 3000$ T, which is comparable to the 2000 T seen.

In the 2D scaling laws described in Sec. III B and in the sheath-expansion model in Sec. III C, the $\nabla \times \mathbf{B}$ term was neglected in the Ampere-Maxwell equation:

$$\frac{1}{c^2}\frac{\partial \boldsymbol{E}}{\partial t} = -\mu_0 \mathbf{j} + \nabla \times \mathbf{B} \tag{16}$$

To quantify the relative importance of the two terms on the right-hand side to the generation of $\mathbf{E}$ we define the ratio α.

$$\alpha = \frac{\mu_0 j_y}{|\nabla \times \mathbf{B}|} \approx 1. \tag{17}$$

Note that to derive this it was assumed that $j_y = n_f e c$, $B = E_y/c$, and varied on a length scale $L = c/\omega_{\mathrm{pf}}$. Both terms in the Ampere-Maxwell equation are important in the generation of the sheath field.

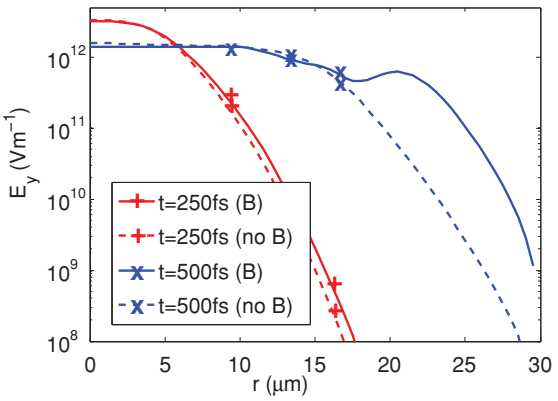

FIG. 6. (Color online) The sheath-field profile along the rear surface with the magnetic field turned on (B—solid lines) and off (no B—dashed lines) after 250 fs (red) and 500 fs (blue).

Although the $\nabla \times \mathbf{B}$ term does therefore modify the rate of generation of E_y at the sheath-field expansion front, it does not dramatically modify the speed of propagation of this front (both sheath-field generation terms only become active when the fast-electron beam from the injection point reaches a given point on the rear) or the magnitude of the saturated sheath; neglecting it was justified in the sheath model. This is demonstrated in Fig. 6, which shows the results of a 2D simulation identical to those presented in Sec. III B but with the magnetic field set to zero for the duration of the simulation. We see that the sheath field was modified, moving slightly slower, but that the overall dynamics was not dramatically altered.

Although we have discussed the effect of the rear-surface B field on the propagation of the sheath E field, we have yet to elucidate its effect on the trajectory of the fast electrons. In order to do this, representative particles were tracked in the 2D simulation with the rear surface included. The tracks for 1-MeV particles injected after 50 fs (chosen to give the B field time to form) are shown in Fig. 7. This figure demonstrates that although there is evidence of the 1-MeV electrons gyrating in the sheath B field, they do not perform $\mathbf{E} \times \mathbf{B}$ drifts along the target's edge. The simple approximation that the E and B fields are constant over the region $0 < y' < \lambda_{Df}$ would lead us to expect this. This field configuration yields a trajectory where the electron enters the region, performs a half gyration, and leaves the region, reentering the (relatively) field-free target. In the absence of sufficiently large fields in the target or B-field gradients, drifts are not significant.

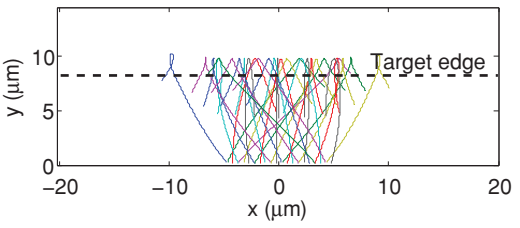

FIG. 7. (Color online) Particle tracks for 1-MeV electrons injected at various angles. The tracks display each particle's motion in the time interval 50–100 fs.

V. MEASURING THE PROPERTIES OF THE FAST-ELECTRON BEAM

In this paper a model has been developed for the generation of the sheath field at the rear surface of the solid target. Centrally important to this model is that fact that the electric field is not strongly dependent on the number of incoming fast electrons. Despite this, careful probing of the sheath has the potential to aid in the characterization of the fast-electron beam's properties. Such measurements have rarely been enlisted for this purpose, whereas measurements of the fast electron's number density and the background temperature are regularly employed. These measurements, in particular that of the temperature, are affected by the presence of the sheath at the rear surface, the electric field of which reflects the fast electrons and causes them to reflux transversely down the target; the fact that the sheath spreads very rapidly transversely along the target means that the rear surface acts like a perfectly reflecting boundary. The utility of measuring these various quantities will be discussed in this section.

A. Temperature and density measurements

The injection angle of the fast-electron beam is often inferred from number density (usually from radiation emitted by the fast electrons at the rear surface, or within a tracer layer inside the target) or temperature measurements at the rear surface [4,5]. These measurements can be strongly affected by refluxing. Figure 8 shows the spatial distribution of the fast-electron number density n_f, 1 ps into the interaction, from the 2D simulations with the reflective boundary at the rear surface (such a boundary was found to be sufficient for determining the conditions inside the target). The upper plot in Fig. 8 shows that the fast electrons were widely spread in the target owing to recirculation. However, the lineout at the rear surface shows that n_f was strongly peaked over 20 μm there, giving a good indication of the lateral extent of the beam. The rate of Ohmic heating is given by

$$\frac{\partial T_e}{\partial t} \propto T_e^{-3/2}. \tag{18}$$

This rapidly saturates as the background temperature T_e increases, so the temperature profile was much broader than the fast-electron number density profile. We expect larger injection angle measurements when diagnosing T_e than n_f: This is consistent with the experimental result of Lancaster *et al.* [4]. As stated previously, FIDO has the ability to suppress recirculation. When this was done the temperature profile narrowed (as did that of n_f, although not as markedly) so that it may be used to give a good half-angle divergence measurement: 30° without refluxing and 70° with refluxing compared to the 28° divergent beam injected (calculated using the profiles in Fig. 8 giving temperature half widths of 10 and 40 μm). This is consistent with the observations of Lancaster *et al.* [6]. A limitation of density and temperature measurements is that it is difficult to use them to infer anything other than the average properties of the beam. However, in principle they may be combined with probing of the sheath to yield more information about the fast electron's distribution function.

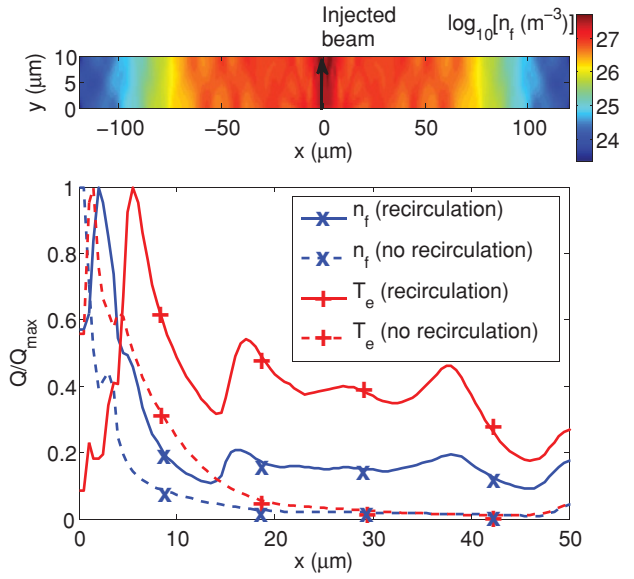

FIG. 8. (Color online) Logarithm of the fast-electron number density after 1 ps (top). Relative change in fast-electron number density and background electron temperature ($Q/Q_{\max}$) along the rear of the target after 1 ps (bottom). The maximum number density and temperature on the rear surface were 4.6×10^{27} m^{-3} and 690 eV with recirculation and 3.8×10^{27} m^{-3} and 530 eV without recirculation.

B. Using the sheath field to measure the angular divergence (and average energy)

We have seen that the saturated sheath field has peak value E_y^{peak} and scale length λ_{Df} given by $E_y^{\text{peak}}\lambda_{Df} = T_f$. Therefore, it should be possible, by measuring these two quantities (using proton probing, as used recently by several authors [22,25]) to determine the number of fast electrons and their average energy at a point on the rear surface and thus to reconstruct their angular distribution in both number and energy. In fact, this is the reverse of the process in discussed in Sec. III B, where scaling laws for E_y^{peak} were used to reconstruct its profile from n_f; therefore it is possible to reconstruct n_f and T_f from E_y^{peak} and the scale length λ_{Df} by using the following formulas:

$$T_f = E_y^{\text{peak}}\lambda_{Df}, \quad n_e = \frac{\epsilon_0 \left(E_y^{\text{peak}}\right)^2}{T_f e^2}. \tag{19}$$

The advantage of using the sheath to probe n_f over direct measurement (as discussed in the previous section) is that $E_y^{\text{peak}} \propto n_f^{1/2}$. Thus the sheath is sensitive to relatively low beam densities and can yield a measurement of the number of fast electrons injected at large angles over a broad region of the target. If there are many electrons injected at large angles, the beam may not self-collimate, with serious consequences for fast ignition.

As a proof of principle, simulations identical to those in Sec. III B where the sheath field was resolved in 2D but where the injection function was modified were performed. The resulting sheath fields were used to reconstruct the electron's average energy and number density along the target's rear surface. The reconstructions were made using E_y^{peak} and Φ—in

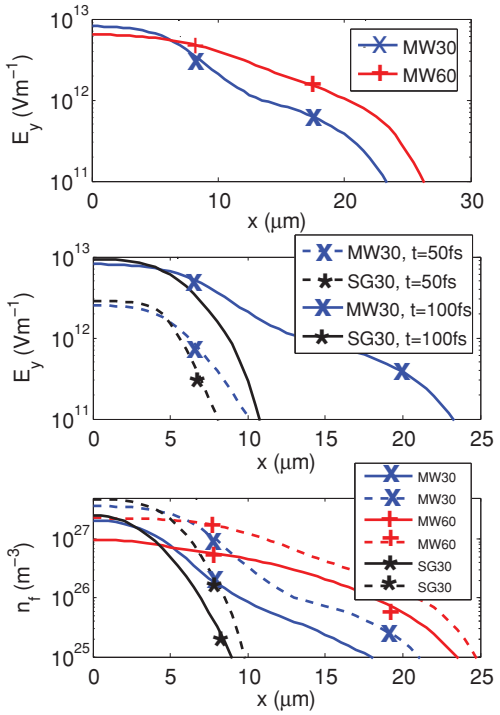

FIG. 9. (Color online) Comparison between the lateral sheath-field profile for injected distributions with average half angles of 30° and 60° after 100 fs (top) and between the sheaths for an injected Gaussian $m = 2$ and super-Gaussian $m = 50$ (middle). The densities reconstructed for each case (dashed lines) compared to that from the simulation (solid lines) after 100 fs (bottom).

principle λ_{Df} could have been used instead. The injection function was modified to

$$f_{\mathrm{inj}}(p,\theta)^* \propto \exp\left[-\left(\frac{\theta}{\theta_{1/2}}\right)^m\right]. \tag{20}$$

The following cases were simulated:

$$\begin{aligned} &\text{MW30:} \quad m = 2 \quad \theta_{1/2} = 30^\circ; \\ &\text{MW60:} \quad m = 2 \quad \theta_{1/2} = 60^\circ; \\ &\text{SG30:} \quad m = 50 \quad \theta_{1/2} = 30^\circ. \end{aligned}$$

The case with $m = 50$ represents a step function in θ, as used in Ref. [26]. The top and middle plots in Fig. 9 show that the sheath field does reflect the differences in the distribution function in each case. The top plot shows that the sheath is stronger over a wider range of x when the average half angle is increased, i.e., when the beam is more spread out. When the distribution function had a sharp cutoff in angle, the speed of the lateral spreading was greatly reduced, as shown in the middle plot. This was owing to the number density of fast electrons quickly falling so low that the sheath setup time became longer than 100 fs; recall that the setup time is $\tau_s = 1/\omega_{\mathrm{pf}} \propto n_f^{-1/2}$. The bottom plot in Fig. 9 shows that the number density of electrons can be reconstructed to within an average error of a factor of 2 using Eqs. (19). Finally note that the measurements of the sheath allow the (spatially resolved) average energy of the electrons to be measured; a full discussion of this is left as further work.

VI. DISCUSSION

A. Measuring the properties of the injected beam

Characterization of the fast-electron beam plays a vital part in understanding ultrahigh-intensity laser-solid interactions. Currently this is often done by making temperature or density measurements that are in general not sensitive to the detailed structure of the fast electron's distribution function and that may not even yield accurate measurements of the average injection angle owing to refluxing currents heating the target over a large volume. The sheath field causes ion acceleration (as will be discussed in more detail in the next section); however, anomalously large ion-emission regions have been observed that, if assumed to be indicative of the beam size, give an estimate of the injection angle that is inconsistent with the results of temperature and density probing. In this paper the discrepancy in the angular divergence between various diagnostics has been shown to be as expected—we would expect density measurements to yield the smallest value, temperature measurements a larger value, and ion-spot size the largest. We have demonstrated that this can be overcome if specially shaped targets are shot, as was done experimentally by Lancaster *et al.*, reducing volumetric Ohmic heating caused by refluxing, and if the sheath field is interpreted correctly.

The elucidation of the ion-static sheath field provided here suggests a way that several important parameters of this distribution can be measured. By diagnosing the peak electric field and its scale length using proton probing, in the absence of refluxing, the number density and average energy of the fast electrons can be spatially resolved, potentially constraining their injected distribution. Note that the sheath actually reveals the distribution of fast electrons along the rear of the target, thus modification to the beam's distribution occurring inside the target (for example, by collimating B fields) needs to be taken into consideration.

That spatially and temporally resolved proton probing of the sheath is possible has been demonstrated recently by the deployment of such a diagnostic by Quinn *et al.* [22] The great advantages of such a diagnostic are as follows: that it has a very large dynamic range, probing current densities that are very small fractions of the maximum value, i.e., 10^{-6}, and because the sheath's potential only depends on its energy, decoupling measurements of the beam's energy from its density (for comparison, diagnosing the temperature measures the energy density of the beam). Measuring the energy of the beam is also crucial to determining the viability of fast ignition.

There are two caveats in the use of such a probing technique; the first is that the sheath field probed must be the ion-static sheath, as will be discussed in the next section. One must measure the sheath before ions are accelerated. Second, the fast-electron Debye length can be very small (the minimum value was 0.2 μm in the simulations described in this paper). The plateau has a much longer scale length; consequently it is important to be sure which part of the sheath is being probed to correctly interpret its measurement, particularly because the plateau does not necessarily yield information about the fast-electron beam inside the target.

An attempt to measure the superluminal expansion of the sheath field would provide a definitive experimental test of the

sheath model presented here and so its use in characterizing the fast electron's distribution function. Several experiments have observed ion-emission regions large enough that the expansion speed must be $\approx c$; however, the region over which superluminal expansion should occur can often be too small to measure. This is the case in several experiments where lateral expansion at $\approx c$ has been observed [10,22]. Equation (14) can be rearranged to yield

$$v_E = c\left(1 + \frac{L^2}{x^2}\right)^{1/2}, \tag{21}$$

where x is the transverse distance along the rear surface. For a given target thickness we might expect to observe superluminal expansion when $L/x > 1$. For 10-μm targets this only occurs within the first 10 μm from the laser axis. To see superluminal speeds, thicker targets need to be used.

Finally, if there is a low-density gap between the cone tip and the compressed DT core in fast ignition, the superluminal sheath field spreading will be relevant. Such rapid field dynamics will lead to strong sheath fields extended over large areas of the cone tip, preventing the fast-electron beam escaping the cone.

B. The consequences for ion acceleration

The sheath-field dynamics discussed in this paper is important for understanding the TNSA ion-acceleration mechanism, but care must be taken to note that the ion-accelerating sheath is significantly modified as the ions are accelerated. The sheath field moves from the ion-static phase to the plasma-expansion phase, which exhibits quite different behavior, as was described by Mora [27]. The development of the sheath field before the ions move initiates ion acceleration, therefore, the size of the ion-emitting region should correspond to the lateral extent of the ion-static sheath, so we can apply the sheath model here to some aspects of TNSA.

The rapid expansion of the sheath seen here indicates a rapidly growing ion-acceleration region. In addition, the primary importance of electrons on their first pass through the target to the generation of the sheath meant that the sheath's extent was more dependent on the injection function than the level of refluxing. Therefore, the size of the ion-emitting region should be relatively independent of the amount of refluxing and so it should not depend strongly on the thickness of the target. What one cannot predict from the ion-static sheath model is that the number of accelerated ions is proportional to the number of fast electrons [27]. Therefore, the flux of ions should fall rapidly with distance from the laser spot. In addition, refluxing will make a large difference to the ion flux by dramatically increasing the fast-electron flux far from the injection region. Therefore, we expect that the main difference in ion emission from thin targets, where refluxing is significant, and thick targets, where it is not, should only be in the flux of ions emitted, that being much lower in the latter case.

Understanding the insensitivity of the initiating sheath field to n_f means that we may tune the ion emission to suit the desired practical application. If a large emission region is required then defocusing the laser may be beneficial—the less strongly beamed fast electron population will generate a larger accelerating structure on the rear surface.

VII. CONCLUSIONS

In laser-solid interactions it is frequently the case that one is interested in processes occurring at the rear of the target or probing it to infer the conditions inside the target. In this paper it was shown that an adequate treatment of the rear surface and, in particular, including the sheath field was crucial to interpreting measurements of the fast electrons beam's divergence and to understanding the sheath-field expansion in ion acceleration. An adequate model for the sheath needs to be considered when interpreting the majority of short-pulse laser-plasma experiments and simulations. As a result of resolving the sheath field generated by very low incident fast-electron-beam densities, a simple Debye sheath model was shown to be sufficient. From this we conclude the following:

(1) The sheath field's initial expansion was controlled by electrons on their first pass through the target, causing superluminal lateral expansion of the field, as is consistent with the rapid expansion seen in experiments.

(2) Almost all electrons incident on the rear -surface were reflected owing to the large lateral extent of the sheath caused by its rapid spreading. The background electron temperature was shown to overestimate the divergence owing to its broadening by this recirculation. Disabling recirculating currents using specially shaped targets dramatically improved the measurement.

(3) The weak dependence of the sheath potential on the incoming number density of electrons means that care must be taken when relating the size of the ion-emission region to the beam properties inside the target, but with careful probing of the sheath unique information can be gained about the details of the fast-electron distribution function.

Correctly modeling the sheath field will be of fundamental importance to many experiments not considered in detail in this paper. Measurements of the electron's energy distribution depend on those electrons that escape the sheath field; in the same way the energy of any positrons produced in laser-solid interactions will be dramatically modified by the sheath.

ACKNOWLEDGMENT

This work was funded by the HiPER project and the Imperial College Centre for Inertial Fusion Studies.

[1] M. Tabak *et al.*, Phys. Plasmas **1**, 1626 (1994).
[2] S. C. Wilks *et al.*, Phys. Plasmas **8**, 542 (2001).
[3] J. J. Honrubia, C. Alfonsín, L. Alonso, B. Pérez, and J. A. Cerrada, Laser Part. Beams **24**, 217 (2006).
[4] K. L. Lancaster *et al.*, Phys. Rev. Lett. **98**, 125002 (2007).
[5] J. S. Green *et al.*, Phys. Rev. Lett. **100**, 015003 (2008).
[6] K. L. Lancaster *et al.*, Phys. Rev. E **80**, 045401(R) (2009).
[7] M. Zepf *et al.*, Phys. Plasmas **8**, 2323 (2001).

[8] M. Zepf *et al.*, Phys. Rev. Lett. **90**, 064801 (2003).
[9] R. A. Snavely *et al.*, Phys. Rev. Lett. **85**, 2945 (2000).
[10] P. McKenna *et al.*, Phys. Rev. Lett. **98**, 145001 (2007).
[11] T. E. Cowan *et al.*, Phys. Rev. Lett. **92**, 204801 (2004).
[12] Romangnani *et al.*, Phys. Rev. Lett. **95**, 195001 (2005).
[13] M. Sherlock, Phys. Plasmas **16**, 103101 (2009).
[14] A. Pukhov, Phys. Rev. Lett. **86**, 3562 (2001).
[15] A. R. Bell *et al.*, Plasma Phys. Controlled Fusion **39**, 653 (1997).
[16] A. R. Bell *et al.*, Plasma Phys. Controlled Fusion **48**, R37 (2006).
[17] R. J. Kingham and A. R. Bell, J. Comp. Phys. **194**, 1 (2004).
[18] P. Collela and P. R. Woodward, J. Comp. Phys. **54**, 174 (1984).
[19] R. Evans, High Energy Density Phys. **2**, 35 (2006).
[20] L. Spitzer and R. Harm, Phys. Rev. **89**, 977 (1953).
[21] H. M. Milchberg, R. R. Freeman, S. C. Davey, and R. M. More, Phys. Rev. Lett. **61**, 2364 (1988).
[22] K. Quinn *et al.*, Phys. Rev. Lett. **102**, 194801 (2009).
[23] D. W. Forslund and J. U. Brackbill, Phys. Rev. Lett. **48**, 1614 (1982).
[24] M. Passoni, V. T. Tikhonchuk, M. Lontano and V. Yu. Bychenkov, Phys. Rev. E **69**, 026411 (2004).
[25] L. Willingale *et al.*, Phys. Plasmas **17**, 043104 (2010).
[26] J. R. Davies, J. S. Green, and P. A. Norreys, Plasma Phys. Controlled Fusion **48**, 1181 (2006).
[27] P. Mora, Phys. Rev. Lett. **90**, 185002 (2003).